Optimizing Weekly-Period Cyclical Lockdown Policies: A Simulation Study Using the A-SIR Model

Arief Anbiya[1], **Benny Yong**[2,*]

[1]Independent Researcher, Tangerang Selatan 15229, Indonesia
[2]Center for Mathematics and Society, Department of Mathematics, Parahyangan Catholic University, Bandung 40141, Indonesia

[*]Email: benny_y@unpar.ac.id

Abstract

This paper presents numerical simulations of a COVID-19 cyclical lockdown scenario characterized by alternating short phases of "working days" or free activity and lockdown days within a weekly cycle. We employ an adaptive SIR compartmental model with daily-varying transmission and recovery rates, fitted to U.S. COVID-19 data. The rates used for model fitting are estimated using the Method of Variational Imbedding (MVI) combined with fixed-point iterations based on observed COVID-19 data. Using this adaptive model, we simulate cyclical lockdowns with W "working days" (normal state) and L lockdown days, subject to the weekly constraint $W + L = 7$. To represent the intervention, the transmission rate is scaled by a piecewise continuous damping function taking the value 1 during "working days" (no lockdown) and 0.175 during lockdown days. The simulations show that allowing up to five "working days" per week can flatten the curve of active cases. We also compare cyclical lockdowns against prolonged, constant-level lockdowns. The results indicate that a prolonged, constant-level lockdown without intermittent "working days" can produce smaller final epidemic size. Moreover, such lockdowns are most effective when concentrated during periods of high transmission. However, as the number of lockdown days L increases, the cyclical lockdown outcome converges to that of a constant-level lockdown in terms of the final epidemic size. Although the continuous lockdown achieves a slightly smaller total incidence, the difference is not substantial. This suggests that cyclical lockdowns may offer a reasonable trade-off, balancing epidemic control with social and economic benefits. The Octave codes for data processing, MVI estimation, and cyclical lockdown numerical simulation are publicly available (see Data and Code Availability section).

Keywords: COVID-19, cyclical lockdown, adaptive SIR model, method of variational imbedding

2020 MSC classification number: 92D30, 93C95, 65L09, 34C60

1. INTRODUCTION

As demonstrated during the recent COVID-19 pandemic, dynamic and effective policies are critical for mitigating the impact of infectious diseases. While prolonged stay-at-home orders and mobility restrictions can suppress disease transmission, they also impose significant social and economic costs [1], [2], [3]. Thus, alternative measures that are less disruptive than strict and prolonged lockdowns should be considered. One way to evaluate the effectiveness of such strategies is through epidemiological modeling. An alternative strategy of interest in this paper is short-term or fast cyclical lockdowns: an alternating phase between short-term lockdowns and short-term normal activities. To assess this strategy, we develop an adaptive SIR (A-SIR) model and conduct simulations. The A-SIR model incorporates dynamic, daily-varying transmission and recovery rates, denoted by $\beta(t)$ and $\alpha(t)$. In addition, we also compare the results from short-term cyclical lockdowns with the results from traditional prolonged lockdowns.

Several studies have explored mathematical models of Non-Pharmaceutical Interventions (NPIs), including lockdown measures. For diseases other than COVID-19, prior research [5], [4], [6] has demonstrated the effectiveness of various control strategies in reducing the burden of measles, mpox, and dengue fever. Theoretical work using compartmental epidemic models has also examined optimal lockdown strategies aimed at minimizing total incidence during an epidemic [7], [8]. In [9], the effects of major interventions—including

[*]Corresponding Author

Received April 21^{st}, 2025, Revised August 25^{th}, 2025, Accepted for publication March 5^{th}, 2026. e-ISSN: 2549-2896, DOI:10.5614/cbms.2026.9.1.7

school closures and nationwide lockdowns—across 11 European countries up to 4 May 2020 were analyzed. Using a backward modeling approach based on observed deaths (informed by an infection-to-death distribution), the study concluded that lockdowns were highly effective in suppressing disease transmission.

Numerous simulation and numerical studies have examined COVID-19 lockdown strategies using compartmental models. In [10], a Susceptible–Asymptomatic–Infected–Recovered (SAIR) model was applied to analyze the impact of short-term lockdowns. The authors introduced a control law defined by a time-dependent expression that depends linearly on the number of infected individuals $I(t)$ and its derivative $I'(t)$. They used two different constant transmission rates: one for the normal state and another for the lockdown state. Similarly, in [11], a modified SIDHARTE model was used to simulate a Fast-Periodic-Switching-Policy (FPSP). In this framework, the transmission rate alternates periodically, modeled by a piecewise constant function that takes the value 0.175 during lockdown and 1 otherwise. In [12], a Susceptible–Vaccinated–Exposed–Infected–Quarantined–Hospitalized–Recovered (SVEIQHR) model was proposed to incorporate five intervention strategies implemented by the Indonesian government. Their findings indicated that, if social restrictions were infeasible, vaccination should be prioritized. Likewise, [13] introduced a Susceptible–Infected–Recovered–Vaccinated (SIRV) model to evaluate the combined effects of social distancing and vaccination. The results showed that vaccination alone could substantially reduce transmissions, even in the absence of social distancing. In [14], a Susceptible–Exposed–Infected–Recovered–Deceased (SEIRD) model was integrated with real mobile phone data to represent population mobility. The study introduced a cost functional capturing penalties associated with fatalities, healthcare demand, and economic losses due to mobility restrictions. Optimizing this functional yielded an optimal lockdown strategy. Similarly, [15] studied optimal lockdown policies using an economic–epidemic framework based on Volterra integral equations rather than ordinary differential equations. In [16], a classical SIR model was extended with a two-phase optimization problem. The functional included a utility measure dependent on working hours and consumption, where individuals in each compartment sought to maximize personal utility, while a regulator determined the lockdown policy that maximized aggregate utility. In [17], a multigroup SIR model with heterogeneous transmission, hospitalization, and fatality rates was used to examine targeted lockdowns. The findings suggested that stricter lockdowns for older age groups were more effective than uniform policies. In [18], a Susceptible–Exposed–Infected–Recovered (SEIR) model was used to analyze a population partitioned into three groups: one that remained unconfined throughout the simulation and two that alternated between confinement and deconfinement. A Heaviside function was applied as a damping factor to the constant transmission rate to model these alternating interventions.

As in [11], the periodical or cyclical lockdowns in this paper is defined as the intervention of alternating states between W days of free (or working) activity and L days of lockdown. Here we use weekly period, so that $W + L = 7$. Our paper is distinct from the related studies, since we use an adaptive SIR model (A-SIR) with variable (daily) transmission and recovery rates so that the dynamical system would be more relevant and realistic. In a state of lockdown, we also multiply our transmission rate with 0.175. The daily transmission and recovery rates are estimated based on the method of Variational Imbedding (MVI) as in [19] in particular, which uses a functional and fixed-point iteration method to find the minimum of the functional. Other literatures on MVI can be seen in [20], [21], [22]. Our implementation of the MVI differs from [19]: we added 3 points of artifical data between every two consecutive days (by simple linear interpolation) so that we can estimate the rates daily. Other data-driven estimation of time varying parameters for epidemiological model can also be seen in [23], [24], [25]. Time-varying transmission rate has also been implemented for modelling COVID-19 in [26], [27], although the context is not about cyclical short-term lockdowns.

In [8], a theoretical study on optimal (non-pharmaceutical) intervention strategy that minimizes total incidence or final epidemic size presented a theorem for the optimal piecewise continuous function that can be applied to damp the transmission rate. The theorem is restated in this paper as the following

Theorem 1.1. *Under the "controlled" classical SIR model given by*

$$\frac{dS}{dt} = -(1-u)\beta SI, \quad \frac{dI}{dt} = (1-u)\beta SI - \alpha I,$$

where $u(t) \in [0,1]$ is the control function that reflects an intervention strategy, for any initial state $S(0), I(0) > 0$, the total incidence among all possible piecewise continuous functions $u(t)$ with constraints $\int_0^\infty u(t)dt \leq c_1$

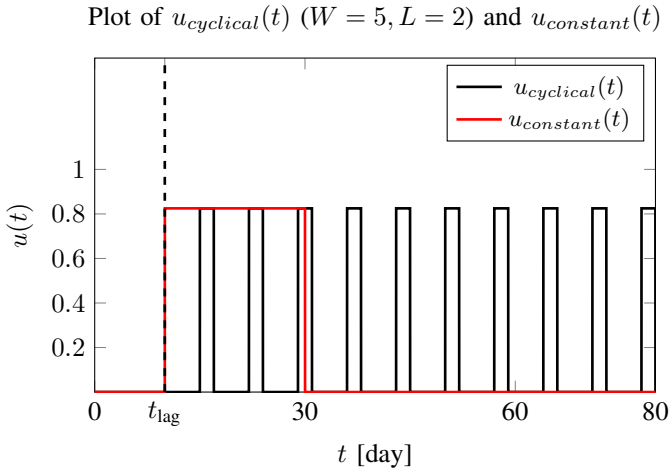

Figure 1: The black line is the $u_{cyclical}(t)$ for the case $W = 5, L = 2$ implemented for 10 weeks with $t_{lag} = 10$. Since 10 weeks mean $10L = 20$ lockdown days, then the control function for the continuous constant-level lockdown (red line) is $u_{constant}(t)$ when $c_\infty = 0.825$ with starting time t_{lag}, and $t_2 = 30$.

and $\sup_{t\geq 0} u(t) \leq c_\infty$ *is minimized by the optimal-choice function of the form*

$$u(t) = \begin{cases} 0, & t \in (0, t_1] \quad (\textit{wait}), \\ c_\infty, & t \in (t_1, t_2] \quad (\textit{suppress}), \\ 0, & t \in (t_2, \infty) \quad (\textit{relax}), \end{cases} \tag{1}$$

with duration $t_2 - t_1 = c_1/c_\infty$*, and a uniquely determined start time* t_1.

The theorem is derived under the classical SIR model [28] with constant transmission and recovery rates. However, we are interested in examining how the optimal control function from the theorem performs when transmission and recovery rates are time-varying. In this paper, we evaluate total incidence through numerical simulations of our cyclical lockdown model and compare it against simulations that apply the same control function of the form (1) (without considering the optimal start time for t_1), but with non-constant rates estimated using the MVI method. Although our results are not general, the objective is to compare the total incidence obtained from (i) simulations using the control function (1), and (ii) simulations of our cyclical lockdown under daily-varying rates. If $t_2 - t_1$ is sufficiently large, the control function (1) corresponds to an intervention equivalent to a prolonged continuous lockdown. Hence, if the difference in total incidence between the two approaches is not significant, cyclical lockdowns may be preferable due to their reduced social and economic burden compared to prolonged lockdowns. The results are summarized in Table 1 and 2.

This paper is structured as follows. Section 2 presents the formulation of the damped A-SIR model, which incorporates time-varying transmission and recovery rates, $\beta(t)$ and $\alpha(t)$. In Section 3, we describe the MVI method used to estimate these rates from real COVID-19 data. We use COVID-19 data in the United States. The initial population size, $N_p = 339.1$ million, is obtained from [29], while the cumulative total cases and daily active cases data are taken from [30]. We set $t = 0$ as 1 March 2020 and set the end of modelling period as 12 April 2024 ($t = 1503$). Section 4 presents the numerical estimation of the transmission and recovery rates and numerical simulations of short-term cyclical lockdowns for different values of W and compares their total incidences with those resulting from the control function (1) without optimizing the starting time. The MVI-estimated rates and the model-fitting are shown in Figure 3. In addition, the transmission rates are compared with different phases of the pandemic in Figure 2.

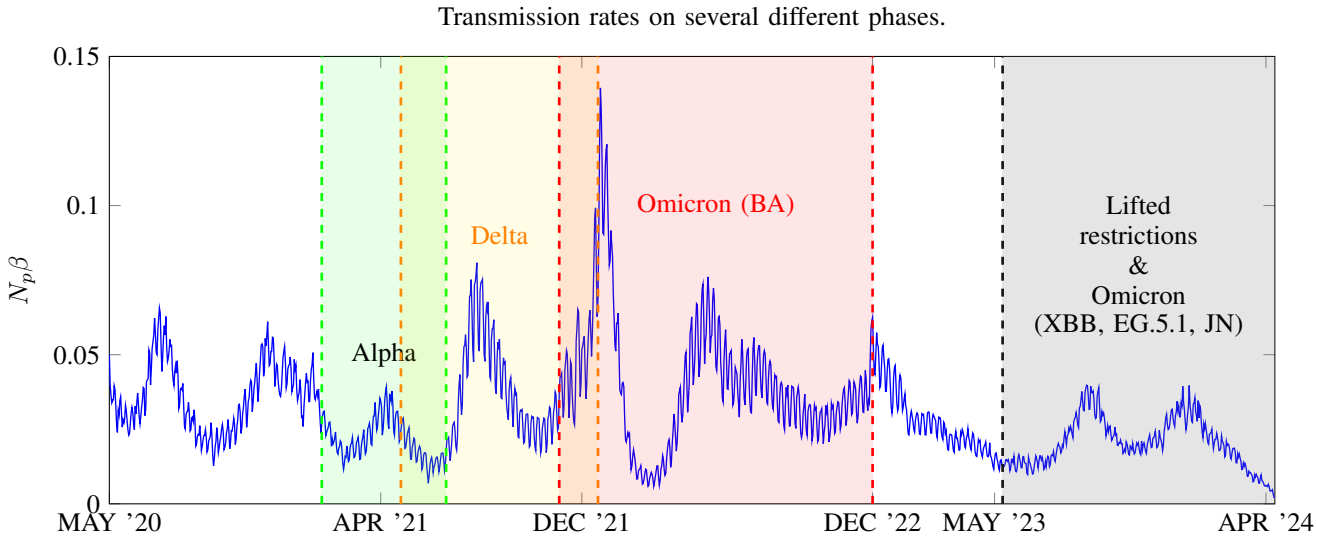

Figure 2: The transmission rates of A-SIR model for United States marked with different phases of Alpha, Delta, and Omicron variants and subvariants.

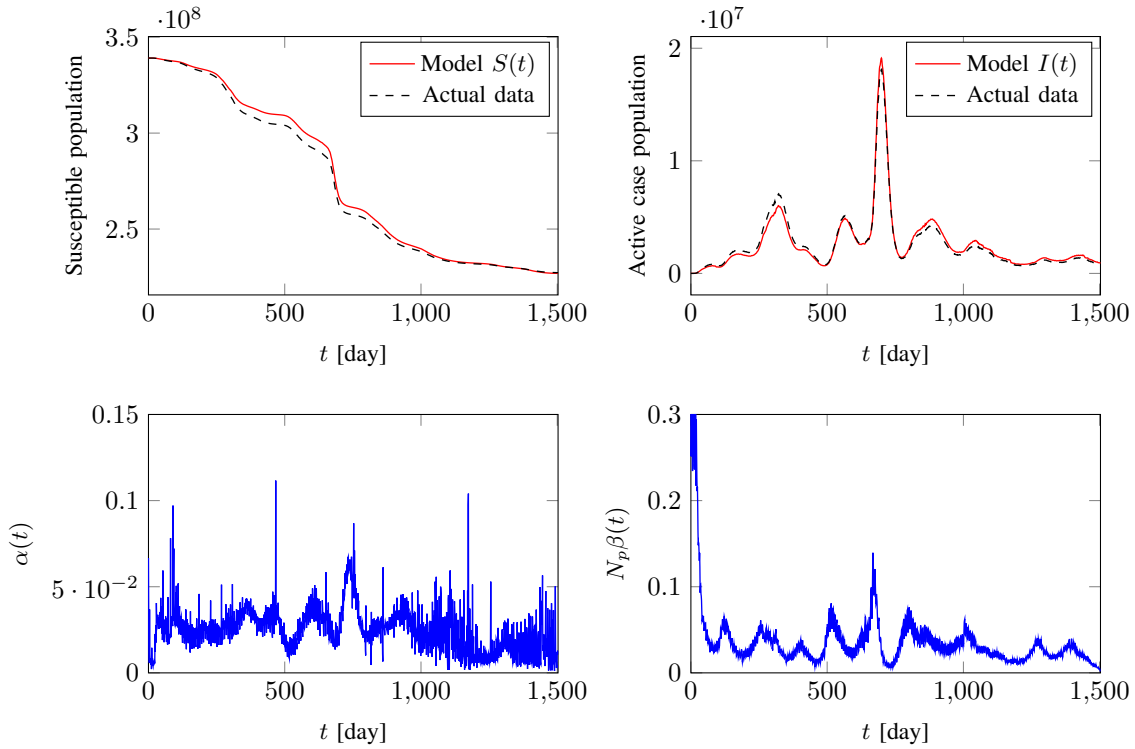

Figure 3: The first row are the plots of S, I using A-SIR model without damping (red lines) compared with the actual data (black dashed lines) for United States. The second row are the MVI-estimated rates.

2. MODEL FORMULATION

Damped A-SIR Model: We consider the following SIR model with non-constant rates

$$\frac{dS}{dt} = -\beta(t)SI, \tag{2}$$
$$\frac{dI}{dt} = \beta(t)SI - \alpha(t)I, \tag{3}$$
$$\frac{dR}{dt} = \alpha(t)I, \tag{4}$$

where $S(t), I(t), R(t)$ are the total number of susceptibles, active cases, and recovered people at time t, respectively. The nonconstant transmission and recovery rates are $\beta(t)$ and $\alpha(t)$, respectively. Let $t_{\text{lag}} \geq 0$ be the starting time of the cyclical lockdown policy, also referred to as lagging time. We define $W \in \{3, 4, 5, 6\}$ and $L = 7 - W$ as the number of "working days" (no lockdown restriction) and the number of lockdown days in a week, respectively. Here, the term "working days" is not limited to regular actual working days, but can also be on weekends or off-days; the emphasis is on the unrestricted activity without lockdown. The cyclical lockdown starts with W "working days" starting from t_{lag} and it is repeated in every interval $[t_{\text{lag}} + 7m, t_{\text{lag}} + W + 7m]$, for $m \in \{0\} \cup \mathbb{Z}^+$. The first lockdown can start at $t_{\text{lag}} + W$ (right after W "working days") and it is impelemented periodically in every interval $(t_{\text{lag}} + W + 7m, t_{\text{lag}} + 7(m + 1))$, for $m \in \{0\} \cup \mathbb{Z}^+$. The damped SIR model is given by the following dynamical systems,

$$\frac{dS}{dt} = -\mathcal{D}(t; W, L, t_{\text{lag}})\beta(t)SI, \tag{5}$$
$$\frac{dI}{dt} = \mathcal{D}(t; W, L, t_{\text{lag}})\beta(t)SI - \alpha(t)I, \tag{6}$$
$$\frac{dR}{dt} = \alpha(t)I. \tag{7}$$

The factor $\mathcal{D}(t; W, L, t_{\text{lag}})$ is our damping function defined as:

$$\mathcal{D}(t; W, L, t_{\text{lag}}) = \begin{cases} 1, & \text{if } , t \in [t_{\text{lag}} + 7m, t_{\text{lag}} + W + 7m], \ \ m \in \{0\} \cup \mathbb{Z}^+, \\ 0.175, & \text{if } , t \in (t_{\text{lag}} + W + 7m, t_{\text{lag}} + 7(m + 1)), \ \ m \in \{0\} \cup \mathbb{Z}^+. \end{cases}$$

Notice that the damping function will suppress the transmission rate $\beta(t)$ to 0.175 every time the short-term lockdown is implemented. Notice that we can also rewrite our cyclical lockdown model (5)-(7) as

$$\frac{dS}{dt} = -(1 - u_{cyclical}(t))\beta(t)SI, \tag{8}$$
$$\frac{dI}{dt} = (1 - u_{cyclical}(t))\beta(t)SI - \alpha(t)I, \tag{9}$$
$$\frac{dR}{dt} = \alpha(t)I, \tag{10}$$

with the control function

$$u_{cyclical}(t) = 1 - \mathcal{D}(t; W, L, t_{\text{lag}}). \tag{11}$$

To the best of our knowledge, since no country implemented cyclical lockdown during the COVID-19 pandemic, we use model (2)-(4) to estimate the rates using the method explained in the next section. After we have obtained the appropriate $\beta(t), \alpha(t)$, we use system (5)-(7) to model and simulate cyclical lockdowns.

Next, we can relate our cyclical lockdown with a constant-level lockdown described in Theorem 1.1. Our cyclical lockdown can be seen as a division of a constant-level lockdown applied on short time intervals with uniform length, see Figure 1. If the cyclical lockdown is implemented for n_{week} number of weeks, then using $u(t) = u_{cyclical}(t) = 1 - \mathcal{D}(t; W, L, t_{\text{lag}})$ will result in $\int_0^\infty u(t)\, dt = 0.825 n_{\text{week}} L$ and $\sup_{t \geq 0} u(t) = 0.825$. Thus the function $u_{cyclical}(t)$ is a piecewise continuous control function under the constraint parameters

$c_1 = 0.825 n_{\text{week}} L$ and $c_\infty = 0.825$. If the Theorem 1.1 can be extended to include for non-constant rates $\beta(t), \alpha(t)$, then there should be a control function of the form

$$u_{constant}(t) = \begin{cases} 0, & t \in (0, t_1] \ \ \text{(wait)}, \\ 0.825, & t \in (t_1, t_1 + n_{\text{week}} L] \ \ \text{(suppress)}, \\ 0, & t \in (t_1 + n_{\text{week}} L, \infty) \ \ \text{(relax)}, \end{cases} \tag{12}$$

with $t_2 = t_1 + n_{\text{week}} L$, such that it produces the minimum total incidence among all possible piecewise continuous functions $u(t) \in [0, 1]$ under the constraints $\int_0^\infty u(t)\, dt \le c_1$ where $c_1 = 0.825 n_{\text{week}} L$, and $\sup_{t \ge 0} u(t) = c_\infty = 0.825$. See Figure 1 for an illustration of the functions (11) (in black color) and (12) (in red color). The result in Table 1 shows that the numerical total incidences by replacing $u_{cyclical}(t)$ in (8)-(9) with $u_{constant}(t)$ (12) are smaller than the total incidences of the cyclical lockdown counterparts for scenarios $L = 1, 2, 3, 4$ with $t_{\text{lag}} = 259$. However, as L increases one can see the difference becomes smaller. Moreover, by changing the lagging time to $t_{\text{lag}} = 289$, we found that cyclical lockdown with $L = 1$ produces lower total incidence than its corresponding constant-level lockdown (see Table 1).

In the next section, we explain how to estimate the daily-varying transmission and recovery rates using the MVI. The MVI involves an inverse problem, numerical minimization of a functional, and fixed-point iterations.

3. Inverse Problem and Minimization

The parameter estimation of $\alpha(t)$ and $\beta(t)$ can be viewed as an inverse problem: given a solution of a system of differential equations (represented by actual COVID-19 data), the objective is to find the suitable functions $\alpha(t)$ and $\beta(t)$ that generate the solution or actual COVID-19 data. First, we set a particular date as $t = 0$, and let $\mathcal{S}_i, \mathcal{I}_i$ be the real-world data of the susceptible population and total active cases, respectively, at day $i \ge 0$. Between two consecutive days, inside interval $[i, i + 1)$, we estimate $\beta(t), \alpha(t)$ as constants β_i, α_i. Therefore, our objective is to look for β_i, α_i for each $i \ge 0$, such that when we use these values in the SIR system (2)-(3), the numerical solution is approximately close to $\mathcal{S}_i, \mathcal{I}_i$ at each i_{th} day.

3.1. Estimating α_i, β_i in Each Interval

We estimate the transmission and recovery rates as constants, daily, on each of the small subintervals $[i, i + 1)$ for $i \ge 0$, one at a time. In between i and $i + 1$, we create artificial data by approximating $\mathcal{S}_{i+0.25}, \mathcal{S}_{i+0.5}, \mathcal{S}_{i+0.75}$ and $\mathcal{I}_{i+0.25}, \mathcal{I}_{i+0.5}, \mathcal{I}_{i+0.75}$ with simple linear interpolations. For each time interval $[i, i+1)$, we aim to find some functions $S(t), I(t)$ and constant parameters β_i, α_i that satisfy the SIR system (2)-(3) and such that $S(t), I(t)$ have the same values as the real-world data points at $t_{i,j} = i + 0.25j$ for $j = 0, 1, 2, 3, 4$. Define

$$L_S(t) = \frac{dS}{dt} + \beta_i SI, \tag{13}$$

$$L_I(t) = \frac{dI}{dt} - \beta_i SI + \alpha_i I. \tag{14}$$

Note that solving the SIR system (2)-(3) is equivalent as solving $L_S(t) = L_I(t) = 0$. We define the functional

$$\mathcal{L}(S, I, \alpha_i, \beta_i) = \int_i^{i+1} \left[(L_S)^2 + (L_I)^2 + \sum_{j=0}^{4} \delta(t - t_{i,j})(S(t) - \mathcal{S}_{t_{i,j}})^2 + \sum_{j=0}^{4} \delta(t - t_{i,j})(I(t) - \mathcal{I}_{t_{i,j}})^2 \right] dt. \tag{15}$$

Here we use the delta-dirac function $\delta(x)$, which is a function that has property $\int_a^b \delta(x - x_0) h(x) dx = h(x_0)$ for any continuous function h, provided $x_0 \in (a, b)$, see [31] for more details about the dirac delta function. Note that the functional (15) has value 0 when $L_S(t) = L_I(t) = 0$ (i.e. when the SIR system is solved) and when $S(t), I(t)$ equal the real-world data points $\mathcal{S}_{t_{i,j}}, \mathcal{I}_{t_{i,j}}$ at $t = t_{i,j}$ (when the solved SIR system equals the actual data at these time points). It is easy to see that $\mathcal{L} \ge 0$, it has minimum value 0 that is attained if and only if $L_S = L_I = 0$, and if $S(t), I(t)$ equal the real-world data points $\mathcal{S}_{t_{i,j}}, \mathcal{I}_{t_{i,j}}$ at $t = t_{i,j}$. Thus, the functions S, I and constants α_i, β_i that minimize (15) to zero also satisfy the SIR system (2)-(3) and conform with the real-world data. Our objective now is to find the functions S, I, and constants α_i, β_i such that the functional (15) is as close as possible to 0.

3.2. Discretization

We minimize (15) in a numerical approach by discretizing the integral. Let $\Delta t = \frac{1}{N}$, where $N+1$ is the number of equally-spaced time points in $[i, i+1)$. The time points is therefore $t_k = i + k\Delta t$, for $0 \leq k \leq N$, and (13) and (14) can be approximated at a particular time $t_k, k \geq 1$, as

$$L_{S,\text{approx}}(t_k) = \frac{S_k - S_{k-1}}{\Delta t} + \beta_i S_{k-\frac{1}{2}} I_{k-\frac{1}{2}}, \tag{16}$$

$$L_{I,\text{approx}}(t_k) = \frac{I_k - I_{k-1}}{\Delta t} - \beta_i S_{k-\frac{1}{2}} I_{k-\frac{1}{2}} + \alpha_i I_{k-\frac{1}{2}}, \tag{17}$$

where $S_k = S(t_k), I_k = I(t_k)$, and

$$S_{k-\frac{1}{2}} = \frac{S_{k-1} + S_k}{2}, \quad I_{k-\frac{1}{2}} = \frac{I_{k-1} + I_k}{2}.$$

Furthermore, the dirac-delta terms in (15) have the approximation

$$\sum_{j=0}^{4} \int_i^{i+1} \delta(t - t_{i,j})(S(t) - \mathcal{S}_{t_{i,j}})^2 \, dt \approx \Delta t \sum_{k=1}^{N} \delta_k (S_k - \bar{\mathcal{S}}_k)^2,$$

$$\sum_{j=0}^{4} \int_i^{i+1} \delta(t - t_{i,j})(I(t) - \mathcal{I}_{t_{i,j}})^2 \, dt \approx \Delta t \sum_{k=1}^{N} \delta_k (I_k - \bar{\mathcal{I}}_k)^2,$$

where we use

$$\delta_k = \begin{cases} \frac{1}{\Delta t}, & t_k = t_{i,j} \\ 0, & t_k \neq t_{i,j} \end{cases}, \quad \bar{\mathcal{S}}_k = \begin{cases} \mathcal{S}_{t_{i,j}}, & t_k = t_{i,j} \\ 0, & t_k \neq t_{i,j} \end{cases}, \quad \bar{\mathcal{I}}_k = \begin{cases} \mathcal{I}_{t_{i,j}}, & t_k = t_{i,j} \\ 0, & t_k \neq t_{i,j} \end{cases}$$

The functional (15) can now be approximated as a function with $2N + 4$ inputs:

$$\Phi(\chi, \alpha_i, \beta_i) = \Delta t \left[\sum_{k=1}^{N} \left(L_{S,\text{approx}}(t_k)^2 + L_{I,\text{approx}}(t_k)^2 \right) + \sum_{k=1}^{N} \delta_k (S_k - \bar{\mathcal{S}}_k)^2 + \sum_{k=1}^{N} \delta_k (I_k - \bar{\mathcal{I}}_k)^2 \right], \tag{18}$$

Where $\chi = \begin{bmatrix} \chi_S \\ \chi_I \end{bmatrix}$, with $\chi_S = [S_0, \ldots, S_N]^T$ and $\chi_I = [I_0, \ldots, I_N]^T$. The problem now becomes finding the vector χ and constants β_i, α_i that sets $\Phi = 0$. However, the function (18) is not guaranteed to be convex over $\mathbb{R}^{2N+4}$, therefore a solution to $\nabla\Phi = 0$ is not necessarily a minimizer such that $\Phi = 0$. So in order to solve $\Phi = 0$, we will use an indirect way by minimizing a slightly modified version of (18), Φ_2, described in the next part. The modified Φ_2 must ultimately converge to Φ at the critical point.

3.3. Linearization

We will define Φ_2 by linearizing the terms (16) and (17) used in Φ. The function Φ_2 will be obtained by changing the *variables* $S_{k-\frac{1}{2}}, I_{k-\frac{1}{2}}$ in (16) and (17) with arbitrary *constants* $\widehat{S}_{k-\frac{1}{2}}, \widehat{I}_{k-\frac{1}{2}}$ for each $k = 0, ..., N$, that are made up by arbitrary *constants* $\widehat{S}_0, \ldots, \widehat{S}_N, \widehat{I}_0, \ldots, \widehat{I}_N$. The nonlinear variable multiplication $S_{k-\frac{1}{2}} \times I_{k-\frac{1}{2}}$ in (16) and (17) now becomes a constant $\widehat{S}_{k-\frac{1}{2}} \times \widehat{I}_{k-\frac{1}{2}}$. Therefore, the only difference between Φ_2 and Φ is that the original uses the nonlinear terms (16) and (17), while Φ_2 uses the linearized terms

$$\Lambda_{S,k} = \frac{S_k - S_{k-1}}{\Delta t} + \beta_i \widehat{S}_{k-\frac{1}{2}} \widehat{I}_{k-\frac{1}{2}}, \tag{19}$$

$$\Lambda_{I,k} = \frac{I_k - I_{k-1}}{\Delta t} - \beta_i \widehat{S}_{k-\frac{1}{2}} \widehat{I}_{k-\frac{1}{2}} + \alpha_i \widehat{I}_{k-\frac{1}{2}}. \tag{20}$$

Hence, we have the following definition

$$\Phi_2(\chi, \alpha_i, \beta_i; \widehat{\chi}) = \Delta t \left[\sum_{k=1}^{N} \left(\Lambda_{S,k}^2 + \Lambda_{I,k}^2 \right) + \sum_{k=1}^{N} \delta_k (S_k - \bar{\mathcal{S}}_k)^2 + \sum_{k=1}^{N} \delta_k (I_k - \bar{\mathcal{I}}_k)^2 \right], \tag{21}$$

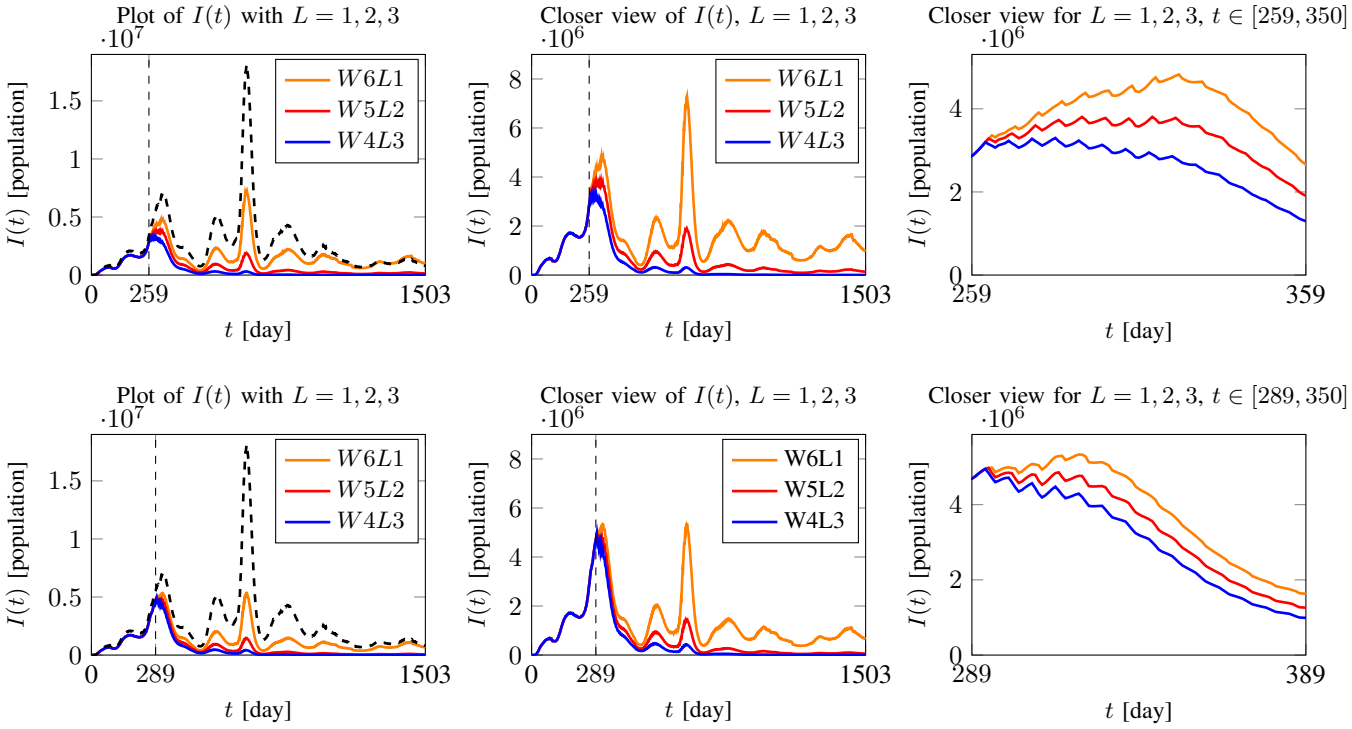

Figure 4: The dynamics of I under various policies: (orange) W6L1, (red) W5L2, (blue) W4L3, with $t_{\text{lag}} = 259$ (first row) and $t_{\text{lag}} = 289$ (second row). The dashed black curve is the actual active case.

where $\widehat{\chi} = \begin{bmatrix} \widehat{\chi}_S \\ \widehat{\chi}_I \end{bmatrix}$, with $\widehat{\chi}_S = [\widehat{S}_0, \ldots, \widehat{S}_N]^T$ and $\widehat{\chi}_I = [\widehat{I}_0, \ldots, \widehat{I}_N]^T$. The function Φ_2 is nonnegative and attains 0 if and only if $\Lambda_{S,k} = \Lambda_{I,k} = 0$ and if the solution vector conforms with the data. Moreover, it is convex. Therefore 0 is the only possible minimum value of Φ_2, and any solution of $\nabla\Phi_2 = 0$ will minimize to 0. The main idea is that once we found some solution vector χ equals, say v, and constants α_i, β_i such that $\Phi_2(v, \alpha_i, \beta_i; \widehat{\chi}) = 0$ (which is done by solving $\nabla\Phi_2 = 0$), we can set our arbitrary constant vector $\widehat{\chi} = v$, and we can do this via fixed-point iterations. This solves $\Phi = 0$, because $\Phi(v, \alpha_i, \beta_i) = \Phi_2(v, \alpha_i, \beta_i; v) = 0$.

We will now solve $\nabla\Phi_2 = 0$. Notice that $\nabla\Phi_2 = [\frac{\partial\Phi_2}{\partial S_0}, \frac{\partial\Phi_2}{\partial S_1}, \ldots, \frac{\partial\Phi_2}{\partial S_N}, \frac{\partial\Phi_2}{\partial I_0}, \frac{\partial\Phi_2}{\partial I_1}, \ldots, \frac{\partial\Phi_2}{\partial I_N}, \frac{\partial\Phi_2}{\partial_{\alpha_i}}, \frac{\partial\Phi_2}{\partial_{\beta_i}}]^T$, so that solving $\nabla\Phi_2 = 0$ is the same as solving $\frac{\partial\Phi_2}{\partial_{\alpha_i}} = \frac{\partial\Phi_2}{\partial_{\beta_i}} = 0$, and solving $\frac{\partial\Phi_2}{\partial S_k} = 0$ and $\frac{\partial\Phi_2}{\partial I_k} = 0$ for each $k = 0, 1, \ldots, N$, simultaneously. We will first solve $\frac{\partial\Phi_2}{\partial S_k} = 0$. One can check that solving $\frac{\partial\Phi_2}{\partial S_k} = 0$ for each k is equivalent as solving the system of linear equations

$$A\chi_S = \mathcal{F}_S(\widehat{\chi}), \tag{22}$$

where the matrix A is

$$A = \begin{bmatrix} -1 & 1 & 0 & \ldots & 0 \\ 1 & -(2 + \Delta t^2\delta_1) & 1 & \ldots & \vdots \\ 0 & \ddots & \ddots & \ddots & 0 \\ 0 & \ldots & 1 & -(2 + \Delta t^2\delta_{N-1}) & 1 \\ 0 & \ldots & 0 & -1 & 1 \end{bmatrix},$$

Table 1: Numerical total incidence or final epidemic size for the cyclical lockdown and the continuous lockdown as a percentage of N_p. The numerical solutions are plotted in Figure 5 and Figure 6.

	$t_{lag} = 259$			$t_{lag} = 289$		
	J (Cyclical)	J (Constant)	t_2	J (Cyclical)	J (Constant)	t_2
L = 1	18.930%	14.740%	436	16.02%	18.15%	462
L = 2	8.716%	3.277%	613	8.89%	4.79%	635
L = 3	5.404%	3.112%	790	6.9%	4.614%	808
L = 4	4.311%	3.111%	967	5.97%	4.613%	981

Table 2: Numerical total incidence or final epidemic size for the cyclical lockdown and the continuous lockdown for the subintervals $[600, 670]$ and $[670, 750]$. The numerical solutions are plotted in Figure 8 and Figure 9.

	Subperiod A ($t_{lag} = 600$)			Subperiod B ($t_{lag} = 670$)		
	$J_{sub,A}$ (Cyclical)	$J_{sub,A}$ (Constant)	t_2	$J_{sub,B}$ (Cyclical)	$J_{sub,B}$ (Constant)	t_2
L = 1	7.25×10^6	8.007×10^6	610	19.19×10^6	9.237×10^6	681
L = 2	4.962×10^6	5.911×10^6	620	14.61×10^6	4.19×10^6	692
L = 3	3.35×10^6	4.175×10^6	630	10.83×10^6	2.69×10^6	703
L = 4	2.241×10^6	2.917×10^6	640	7.89×10^6	2.22×10^6	714

and

$$\mathcal{F}_S(\widehat{\chi}) = \begin{bmatrix} -\Delta t \left(\beta_i \widehat{S}_{\frac{1}{2}} \widehat{I}_{\frac{1}{2}}\right) \\ \Delta t \beta_i \left(\widehat{S}_{\frac{1}{2}} \widehat{I}_{\frac{1}{2}} - \widehat{S}_{1+\frac{1}{2}} \widehat{I}_{1+\frac{1}{2}}\right) - \Delta t^2 \delta_1 \bar{\mathcal{S}}_1 \\ \vdots \\ \Delta t \beta_i \left(\widehat{S}_{N-\frac{3}{2}} \widehat{I}_{N-\frac{3}{2}} - \widehat{S}_{N-\frac{1}{2}} \widehat{I}_{N-\frac{1}{2}}\right) - \Delta t^2 \delta_{N-1} \bar{\mathcal{S}}_{N-1} \\ -\Delta t \left(\beta_i \widehat{S}_{N-\frac{1}{2}} \widehat{I}_{N-\frac{1}{2}}\right) \end{bmatrix}.$$

The solution of (22) is simply

$$\chi_S = A^{-1} \mathcal{F}_S(\widehat{\chi}). \tag{23}$$

Similarly, one can check that solving $\frac{\partial \Phi_2}{\partial I_k} = 0$ for each k is equivalent as solving the system of linear equations

$$A\chi_I = \mathcal{F}_I(\widehat{\chi}), \tag{24}$$

where

$$\mathcal{F}_I(\widehat{\chi}) = \begin{bmatrix} \Delta t \left(\beta_i \widehat{S}_{\frac{1}{2}} \widehat{I}_{\frac{1}{2}} - \alpha_i \widehat{I}_{\frac{1}{2}}\right) \\ -\Delta t \beta_i \left(\widehat{S}_{\frac{1}{2}} \widehat{I}_{\frac{1}{2}} - \widehat{S}_{1+\frac{1}{2}} \widehat{I}_{1+\frac{1}{2}}\right) + \Delta t \alpha_i (\widehat{I}_{\frac{1}{2}} - \widehat{I}_{1+\frac{1}{2}}) - \Delta t^2 \delta_1 \bar{\mathcal{I}}_1 \\ \vdots \\ -\Delta t \beta_i \left(\widehat{S}_{N-\frac{3}{2}} \widehat{I}_{N-\frac{3}{2}} - \widehat{S}_{N-\frac{1}{2}} \widehat{I}_{N-\frac{1}{2}}\right) + \Delta t \alpha_i (\widehat{I}_{N-\frac{3}{2}} - \widehat{I}_{N-\frac{1}{2}}) - \Delta t^2 \delta_{N-1} \bar{\mathcal{I}}_{N-1} \\ \Delta t \left(\beta_i \widehat{S}_{N-\frac{1}{2}} \widehat{I}_{N-\frac{1}{2}} - \alpha_i \widehat{I}_{N-\frac{1}{2}}\right) \end{bmatrix}.$$

The solution is simply

$$\chi_I = A^{-1} \mathcal{F}_I(\widehat{\chi}). \tag{25}$$

Finally, to solve for $\frac{\partial \Phi_2}{\partial_{\alpha_i}} = 0$, $\frac{\partial \Phi_2}{\partial_{\beta_i}} = 0$, we first rewrite the definition Φ_2 in (21) as

$$\Phi_2 = \beta_i^2 \underbrace{\sum_{k=1}^{N} 2\Delta t[\widehat{S}_{k-\frac{1}{2}}\widehat{I}_{k-\frac{1}{2}}]^2}_{C_{20}} + \beta_i \underbrace{\sum_{k=1}^{N}\left[2\left((S_k - S_{k-1}) - (I_k - I_{k-1})\right)\widehat{S}_{k-\frac{1}{2}}\widehat{I}_{k-\frac{1}{2}}\right]}_{C_{10}}$$
$$+ \alpha_i^2 \underbrace{\sum_{k=1}^{N} \Delta t[\widehat{I}_{k-\frac{1}{2}}]^2}_{C_{02}} + \alpha_i \underbrace{\sum_{k=1}^{N}\left[2(I_k - I_{k-1})\widehat{I}_{k-\frac{1}{2}}\right]}_{C_{01}} + \alpha_i\beta_i \underbrace{\sum_{k=1}^{N}\left[-2\Delta t\widehat{S}_{k-\frac{1}{2}}\widehat{I}^2_{k-\frac{1}{2}}\right]}_{C_{11}} + \mathcal{C},$$

where $\mathcal{C}$ is the term that is independent of α_i and β_i. The explicit form of $\mathcal{C}$ does not matter, since the differentiation with respect to α_i, β_i will be 0. Using the above, we obtain the following

$$\frac{\partial \Phi_2}{\partial_{\alpha_i}} = C_{01} + C_{11}\beta_i + 2C_{02}\alpha_i,$$
$$\frac{\partial \Phi_2}{\partial_{\beta_i}} = C_{10} + 2C_{20}\beta_i + C_{11}\alpha_i.$$

Now we must solve $\frac{\partial \Phi_2}{\partial_{\alpha_i}} = \frac{\partial \Phi_2}{\partial_{\beta_i}} = 0$, which is

$$C_{01} + C_{11}\beta_i + 2C_{02}\alpha_i = 0$$
$$C_{10} + 2C_{20}\beta_i + C_{11}\alpha_i = 0.$$

The solution to this elementary system of equations is

$$\beta_i = \frac{2C_{02}C_{10} - C_{01}C_{11}}{C_{11}^2 - 4C_{02}C_{20}}, \quad \alpha_i = \frac{2C_{01}C_{20} - C_{10}C_{11}}{C_{11}^2 - 4C_{02}C_{20}}. \tag{26}$$

We have now achieved χ_S (23), χ_I (25), and α_i, β_i (26) for the solutions of $\nabla\Phi_2 = 0$ and consequently $\Phi_2 = 0$.

Finally, we have mentioned that once we found some solution vector $\chi = [\chi_S, \chi_I]^T$ and constants α_i, β_i such that $\Phi_2(\chi, \alpha_i, \beta_i; \widehat{\chi}) = 0$, we can set our arbitrary constant vector $\widehat{\chi} = \chi$. We can do this via fixed-point iterations, which is described in the next part.

3.4. Fixed-point Iterations

The fixed-point iteration works with the following steps:

1) Set initial guess for the rates $\alpha^*_{m=0}, \beta^*_{m=0}$, and define the recursive sequences $v_{S,n+1} = A^{-1}\mathcal{F}_S(v_n)$ and $v_{I,n+1} = A^{-1}\mathcal{F}_I(v_n)$, where $v_n = \begin{bmatrix} v_{S,n} \\ v_{I,n} \end{bmatrix}$. Note that these sequences relate to (23) and (25).
2) Set initial guess for $v_0 = [v'_S, v'_I]^T$. In this paper, we always use the linear interpolation of the data in interval $[i, i+1]$ as initial guess for every iteration. To be more clear, we always set the initial guess as

$$v'_S = [\mathcal{S}_i, \underbrace{\ldots}_{\text{interpolated}}, \mathcal{S}_{i+0.25}, \underbrace{\ldots}_{\text{interpolated}}, \mathcal{S}_{i+0.5}, \underbrace{\ldots}_{\text{interpolated}}, \mathcal{S}_{i+0.75}, \underbrace{\ldots}_{\text{interpolated}}, \mathcal{S}_{i+1}],$$
$$v'_I = [\mathcal{I}_i, \underbrace{\ldots}_{\text{interpolated}}, \mathcal{I}_{i+0.25}, \underbrace{\ldots}_{\text{interpolated}}, \mathcal{I}_{i+0.5}, \underbrace{\ldots}_{\text{interpolated}}, \mathcal{I}_{i+0.75}, \underbrace{\ldots}_{\text{interpolated}}, \mathcal{I}_{i+1}],$$

with each of the above has $N+1$ elements. Subsequently, we update the two recursive sequences $v_{S,n+1} = A^{-1}\mathcal{F}_S(v_n)$ and $v_{I,n+1} = A^{-1}\mathcal{F}_I(v_n)$ until they numerically converge to a fixed-point with some error tolerance. That is, until the errors $||v_{S,n+1} - v_{S,n}||$ and $||v_{I,n+1} - v_{I,n}||$ very small. For this step, we use error tolerance of 10^{-6}. We call this fixed-point as S_{fix} and I_{fix}. By looking back at (23) and (25), we have now *approximately* solved $\chi_S = A^{-1}\mathcal{F}_S(\widehat{\chi})$ and $\chi_I = A^{-1}\mathcal{F}_I(\widehat{\chi})$ with

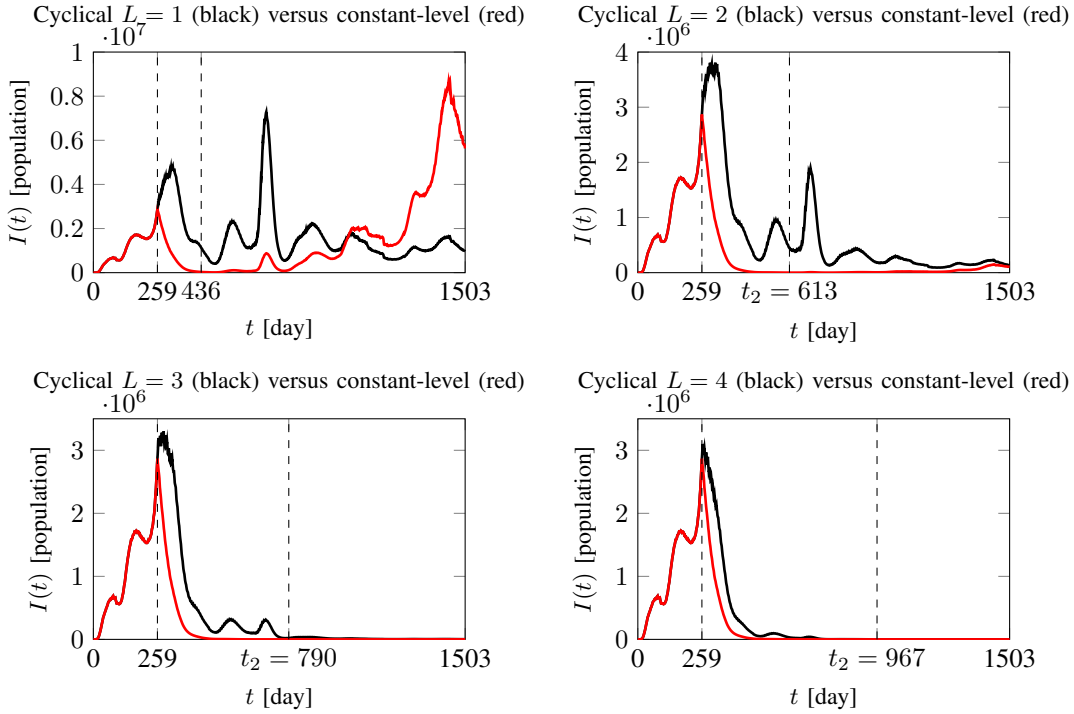

Figure 5: The dynamics of I under constant-level lockdown (red) and cyclical lockdown (black), with $t_{\text{lag}} = 259$.

approximate solutions $\chi_S = \widehat{\chi}_S = S_{fix}$ and $\chi_I = \widehat{\chi}_S = I_{fix}$. Since this *approximately* means $\chi = \widehat{\chi}$, we have *approximately* $\Phi([S_{fix}, I_{fix}], \alpha_m^*, \beta_m^*) = \Phi_2([S_{fix}, I_{fix}], \alpha_m^*, \beta_m^*; [S_{fix}, I_{fix}]) = 0$.

3) Compute new $\alpha_{m+1}^*, \beta_{m+1}^*$ according to (26) using the fixed-point obtained in step 2: by setting $[S_0, \ldots, S_N] = [\widehat{S}_0, \ldots, \widehat{S}_N] = S_{fix}$, $[I_0, \ldots, I_N] = [\widehat{I}_0, \ldots, \widehat{I}_N] = I_{fix}$.
4) If $|\alpha_{m+1}^* - \alpha_m^*|$, and $|\beta_{m+1}^* - \beta_m^*|$ are less than some error tolerance, then we have $\alpha_i \approx \alpha_{m+1}^*$ and $\beta_i \approx \beta_{m+1}^*$ as the estimated rates. For this step, we use error tolerance of 10^{-9}. If not, repeat again from step 2 under the new $\alpha_{m+1}^*, \beta_{m+1}^*$ obtained in step 3.

In general, a fixed-point iteration can be divergent. However, we have tested using initial values of $\alpha_{i,0} = \beta_{i,0} = 10^{-3}$ for each i_{th} day and found the sequences always converge numerically under decent error tolerances. See Theorem 10.6 in [32, p. 633] for convergence condition of fixed-point iteration with multivariable function. In the next section, we discuss the numerical results including the MVI-estimated transmission and recovery rates, cyclical lockdown simulation, and juxtaposition between simulations of cyclical lockdown and constant-level lockdown.

The MVI method is repeated for every two consecutive days. Since in our case we use the United States COVID-19 daily data of 1504 days, this accounts for 1503 times of implementing the fixed-point iterations. In terms of computational efficiency, we obtained the estimated rates shown in Figure 3 under 170 seconds of overall running time, using Octave software [43] in a standard laptop.

4. Numerical Results

In this section, we first discuss the MVI-estimated transmission and recovery rates, before presenting our findings from the cyclical lockdown and constant-level lockdown numerical simulations. All numerical estimations and simulations use discretization with time-step $\Delta t = 10^{-2}$.

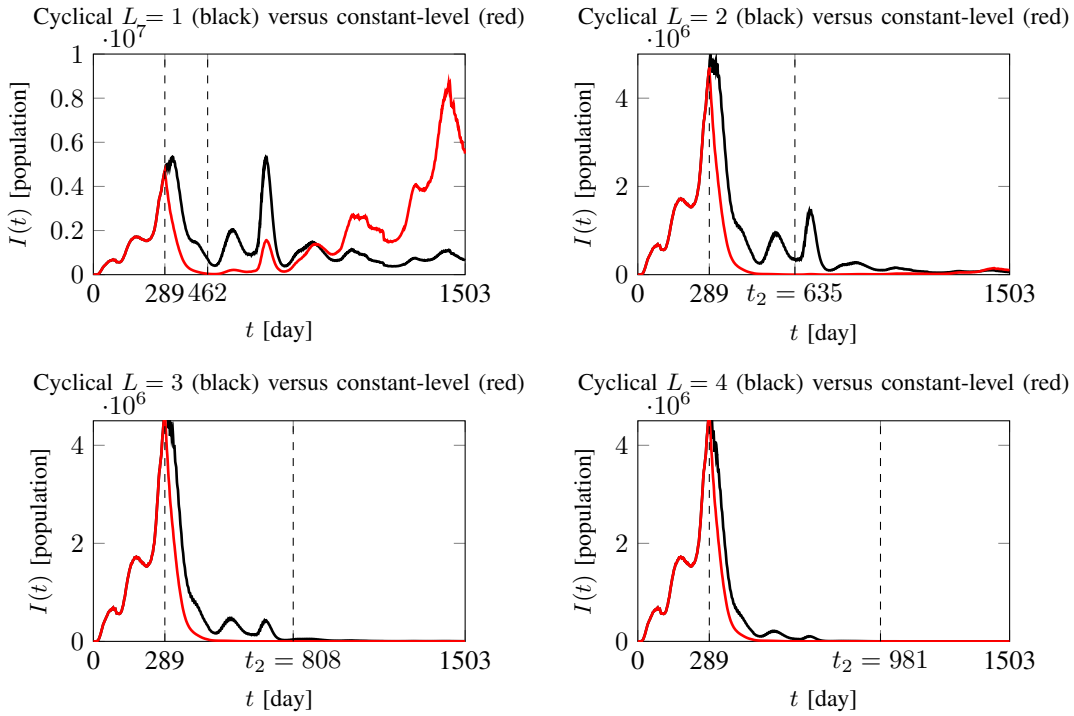

Figure 6: The dynamics of I under constant-level lockdown (red) and cyclical lockdown (black), with $t_{\text{lag}} = 289$.

4.1. MVI-estimated Parameters

We use COVID-19 data in the United States. We set $t = 0$ as 1 March 2020, which means $t = 1503$ is 12 April 2024. In Figure 3, the estimated rates α and $N_p\beta$ are plotted in the second row, while the simulated A-SIR model for United States is compared with the actual data in the first row. Both the daily rates α, β are linearly interpolated between two consecutive days. Using $\Delta t = 10^{-2}$, we have a good approximation for the rates, reflected by the accurate model fitting. In the MVI implementation, note that we first map the actual data to percentages of initial population by dividing them with N_p, which makes the obtained estimated rates valid for $S(t)/N_p, I(t)/N_p, R(t)/N_p$. To model the number of individuals instead of percentage, we only need to divide the MVI-estimated transmission rate by N_p and leave the recovery rate to be the same.

In Figure 2, we also display important periods regarding to the Alpha variant (green region), Delta variant (yellow region), Omicron BA.1 original variant, and its subvariants BA.2,BA.4,BA.5 (red region) of COVID-19. We utilize the data of analyzed sequences of Alpha, Delta, and Omicron variant groups from [33] to estimate the percentage of each variant circulated around specific time points. Approximately, we pick two time points (specific dates) from [33] where each variant started to appear and started to subside. For the United States, the Alpha variant contributed 1.18% of the samples taken by 18 January 2021 ($t = 323$) and then it predominated the samples up to almost 70%, before declining to 42.11% by 21 June 2021 ($t = 477$). The Delta variant started to appear around 26 April 2021 ($t = 421$), with 0.7% of the samples were Delta variant. The Delta variant was dominating among the samples until around 26 December 2021 ($t = 665$), dropping from 75% on 20 December 2021 to 16% on 3 January 2022. The Omicron original variant started to appear around 8 November 2021 ($t = 617$) and then slowly began to dominate until around 1 December 2022 ($t = 1005$). On 5 December 2022, only 39% of the samples were from Omicron (BA), and the dominating group became Omicron (BQ.1) with 55% of the samples. On 11 May 2023, the U.S. administration ends its COVID-19 public health emergency and travel restrictions were lifted [34]. Additionally, between 11 May 2023 and 12 April 2024, Omicron subvariants XBB, EG.5.1, and JN were predominant in different phases. From Figure 2, the transmission wave from Alpha variant is lower than from Delta variant, which is

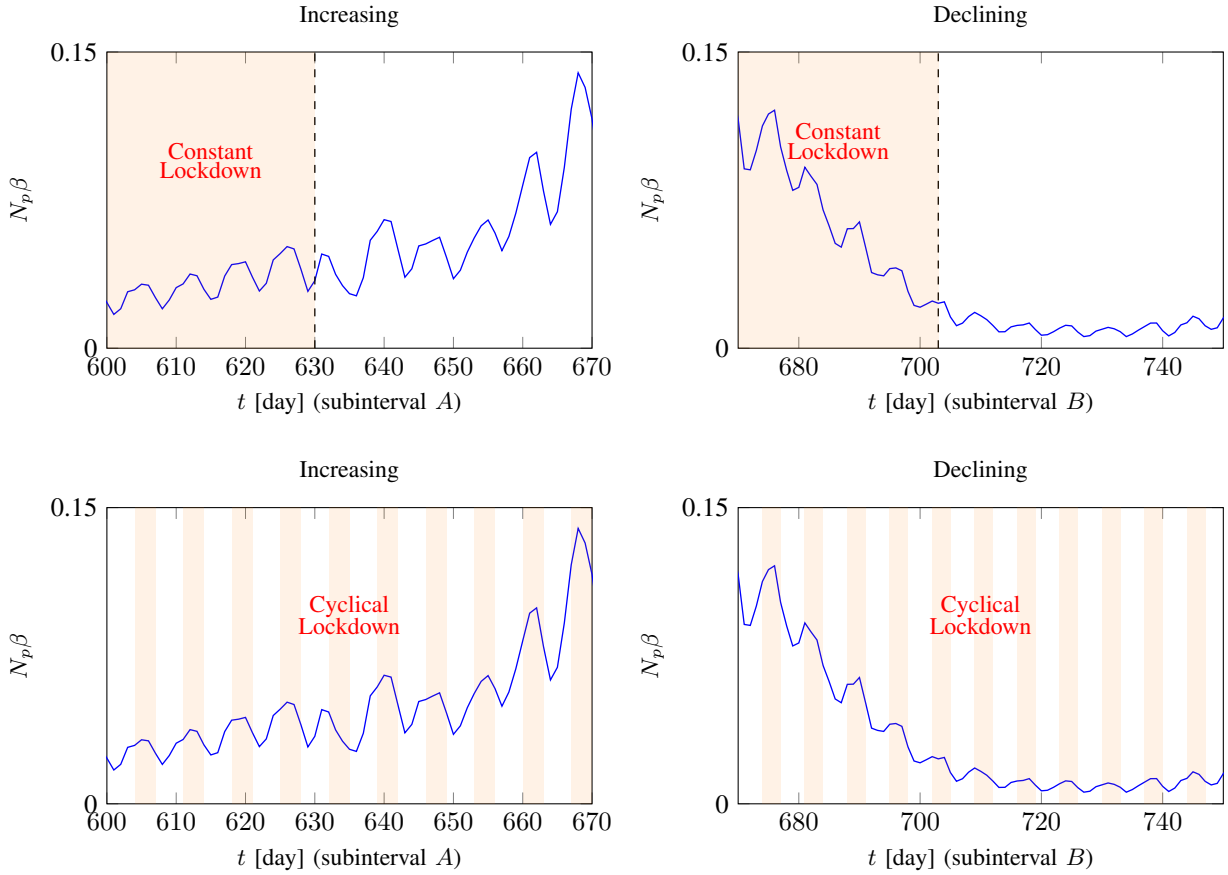

Figure 7: MVI-estimated rates in the subintervals $A = [600, 670]$ and $B = [670, 750]$. This highlights the potential drawbacks of constant-level lockdown in the subinterval A against cyclical lockdown, and shows the possible advantage of constant-level lockdown in the subinterval B against cyclical lockdown. The orange-shaded areas are the time subintervals where constant-level and cyclical lockdowns are implemented.

consistent according to [35]. Moreover, we can see that there is a sharp peak in the beginning of Omicron phase, significantly higher than transmissions during the Delta phase, which is also consistent with [36]–[39].

4.2. Cyclical Lockdown Simulation

Subsequently, using the acquired daily rates for $t \in [0, 1503]$, we do the simulations for the cyclical lockdown scenarios of $L = 1, 2, 3$ that corresponds to $W = 6, 5, 4$ respectively. For all simulations in this paper, we use $\Delta t = 10^{-2}$. We set the lagging time to be the time when the number of actual active cases reaches 1 % of initial population, which leads to $t_{\text{lag}} = 259$. We write $W6L1$ as the scenario of 6 "working days" with 1 lockdown per week. We define $W5L2$, $W4L3$, $W3L4$ in similar manner. As we can see in the first row of Figure 4, we found that the curve of active cases will flatten without encountering a higher peak than $I(t_{\text{lag}})$ for $W \leq 5$. For $W = 6$ the curve forms another high peak (approximately 8 million of active cases) before flattening. Different from [11], our results encourage more "working days" per week: the active case curve in their model only dissipates for the case $W = 0, 1, 2$ "working days" in each weekly period. Additionally, we conduct another test with later lagging time of $t_{\text{lag}} = 289$. This means cyclical lockdown policies start 30 days later than the previous simulations. The results are plotted in the second row of Figure 4. The curve of active cases with $t_{\text{lag}} = 289$ have similar shapes as when $t_{\text{lag}} = 259$, although the peak heights are significantly different. However, both lagging-time scenarios show flattening of the active cases

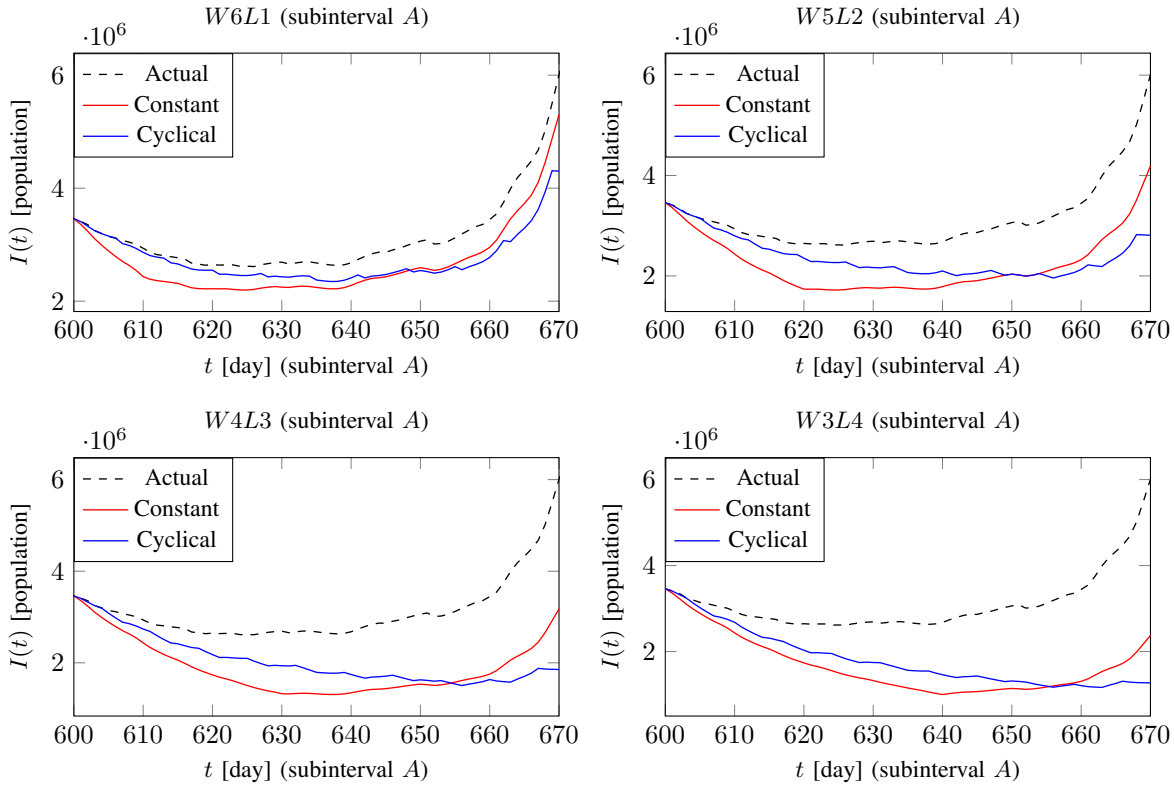

Figure 8: Simulation results of different cyclical lockdown policies (blue) with their corresponding constant-level lockdowns (red) in subperiod A. All lockdown starts at $t_{\text{lag}} = 600$.

for W equals 4 and 5. In the next part, we compare the final epidemic sizes of using cyclical lockdowns against using corresponding constant lockdowns.

4.3. Comparison with Simple Constant-level Lockdown

We now compare the trajectories and total incidences between cyclical lockdown and constant-level lockdown models. As we have discussed in Section 2, the cyclical lockdown can be associated with constant lockdown in terms of the total number of lockdown days. The total modelling period (in days) after $t_{lag} = 259$ is $1503-259 = 1244$, which is tantamount to almost 178 weeks. We take this as 177 weeks, and therefore the scenarios $L = 1, 2, 3, 4$ have total period of lockdown days equal to $177, 354, 531, 708$, respectively. Therefore, for each of the cases $L = 1, 2, 3, 4$, we compare it with the constant-level lockdowns with $c_\infty = 0.825$ and starting time t_{lag}, for each of the cases $t_2 = 436, 613, 790, 967$, respectively. The results are shown in Figure 5. For the case $t_2 = 436$, the number of active cases gradually reach a higher peak at the end than the peak of using cyclical lockdown with $L = 1$. However, the total incidence as a percentage of initial population is 14.74%, and it is still smaller than the total incidence of the cyclical lockdown, which is 18.93%, see Table 1. We computed the numerical total incidence, J, as follows:

$$J = \frac{N_p - S(1503)}{N_p}.$$

The other three simulations show that the constant-level lockdowns manage to consistently flatten the active case curve, but with the expense of longer continuous lockdown. It is important to note that the curve of the cyclical lockdown counterparts seem to converge to the curve of the constant-level lockdown as L increases. The difference between the two is insignificant already for the cases of $L = 3$ and $L = 4$.

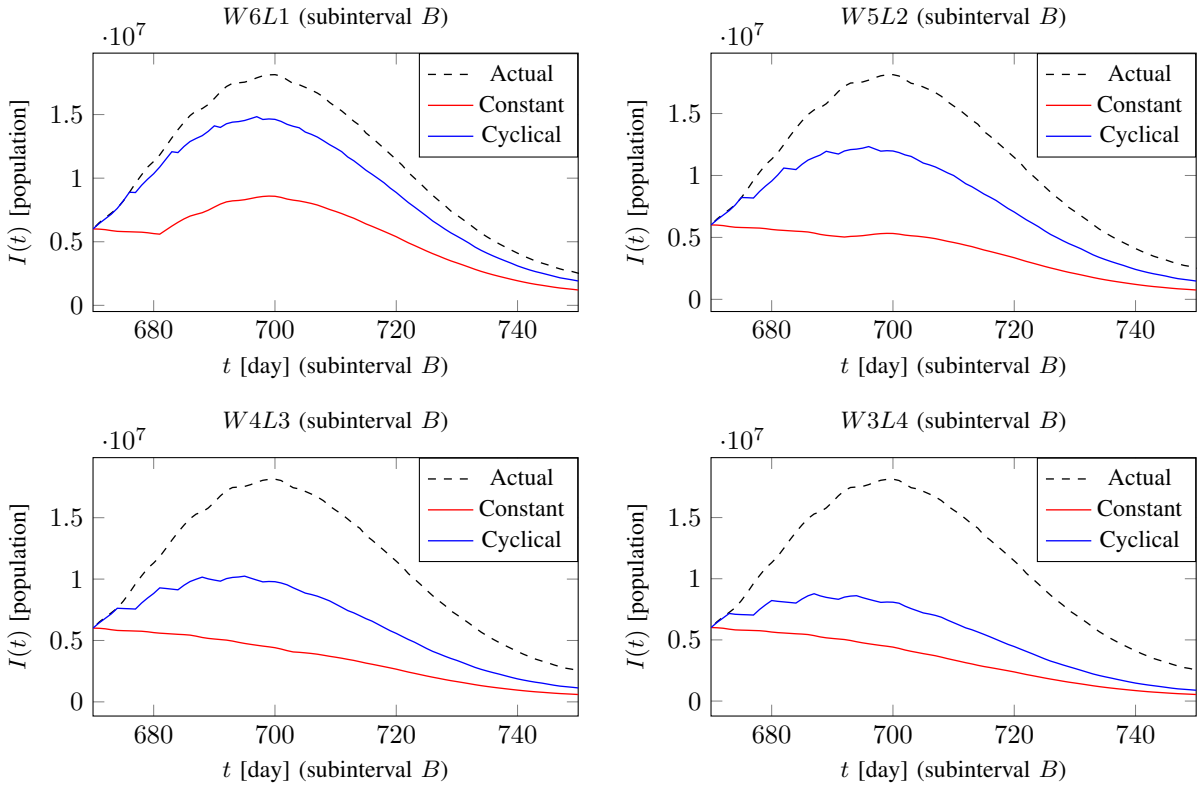

Figure 9: Simulation results of different cyclical lockdown policies (blue) with their corresponding constant-level lockdowns (red) in subperiod B. All lockdown starts at $t_{\text{lag}} = 670$.

We also conduct further simulations by using $t_{\text{lag}} = 289$. The scenarios $L = 1, 2, 3, 4$ have total period of lockdown days equal to $173, 346, 519, 692$, respectively. Therefore, for each of the cases $L = 1, 2, 3, 4$, we compare it with the constant-level lockdowns with $c_\infty = 0.825$ and starting time t_{lag}, for each of the cases $t_2 = 462, 635, 808, 981$, respectively. The results are shown in Figure 6. We found that, for the case $t_2 = 462$, the total incidence percent of using constant lockdown (18.15%) is higher than that of using the corresponding cyclical lockdown with $L = 1$ (16.02%), see Table 1. However, for the other three cases, the constant lockdown has lower total incidence. This curious case can be explained by lockdown timing, which is discussed in the next part.

4.4. Timing of Lockdown Comparison

In Table 1, we see that only when $t_{\text{lag}} = 289$ and $t_2 = 462$, the constant lockdown results in higher final epidemic size than the cyclical lockdown $W6L1$. This might be explained by lockdown timing. Since our transmission rate β is non-constant, some period of times have higher transmission rates than the others. If the constant-level lockdown was implemented on a subperiod with low transmission rates, and lifted when we entered a subperiod of high transmission rates (when the lockdown is actually needed), then using the cyclical lockdown would be more advantageous than using the constant-lockdown. Cyclical lockdown has short-term lockdown periods distributed evenly over the whole period, which makes the high transmission rates more likely to be covered, even though not completely covered. This can be illustrated further in Figure 7, where we look closely for the specific two subperiods where the transmission rate is increasing and declining. We chose these subperiods of increasing and declining transmission to be $t \in [600, 670] = A$ and $t \in [670, 750] = B$, respectively. In the subinterval A, the transmission rate is lower in the beginning,

but sharply increasing until $t = 670$. Thus, if we did a constant-level lockdown starting at $t_{\text{lag}} = 600$, with $t_2 = 630$ for example, then we only suppress the transmission when it was relatively benign and let the comparatively more critical, high transmissions in the second half get away. In this case, we would expect the corresponding cyclical lockdown to be more advantegous. On the other hand, if we did constant-level lockdown in the beginnning of subperiod B, when the transmission rates are relatively high, then we can expect the constant-level lockdown to have lower total incidence than the corresponding cyclical lockdown. To test this, we do further simulations of both cyclical lockdowns and their corresponding constant-level lockdowns inside subperiods A and B separately. Note that the lockdown starting time for subperiod A is $t_{\text{lag}} = 600$, and we do the lockdown simulation only until $t = 670$, and calculate the total incidence happened during that 70 days only. Similarly, note that the lockdown starting time for subperiod B is $t_{\text{lag}} = 670$, and we do the lockdown simulation only until $t = 750$, and calculate the total incidence happened during that 80 days only. The numerical total incidence during the subperiod A is calculated as

$$J_{sub,A} = \begin{cases} \Delta t \sum_{t \in t_A} (1 - u_{cyclical}(t))\beta(t)S(t)I(t), & \text{for cyclical lockdown,} \\ \Delta t \sum_{t \in t_A} (1 - u_{constant}(t))\beta(t)S(t)I(t), & \text{for constant-level lockdown,} \end{cases}$$
$$t_A = \{600, 600 + \Delta t, \ldots, 670 - \Delta t\}.$$

Similarly, the numerical total incidence during the subperiod B is calculated as

$$J_{sub,B} = \begin{cases} \Delta t \sum_{t \in t_B} (1 - u_{cyclical}(t))\beta(t)S(t)I(t), & \text{for cyclical lockdown,} \\ \Delta t \sum_{t \in t_B} (1 - u_{constant}(t))\beta(t)S(t)I(t), & \text{for constant-level lockdown,} \end{cases}$$
$$t_B = \{670, 670 + \Delta t, \ldots, 750 - \Delta t\}.$$

The simulation results for A are plotted in Figure 8, while for B are plotted in Figure 9. The numerical total incidences are summarized in Table 2. From Table 2, the total incidences in subperiod A for cyclical lockdowns are consistently lower than the constant-level lockdowns, as expected. On the other hand, the total incidences in subperiod B for cyclical lockdowns are consistently higher than the constant-level lockdowns. Next, we summarize all findings of this paper in the next section.

5. Concluding Remarks

We will now summarize our findings. We have estimated the non-constant daily transmission and recovery rates for the A-SIR model using actual COVID-19 data, the Method of Variational Imbedding (MVI), and fixed-point iterations. The results of the model fitting demonstrate that this approach can yield a more realistic and relevant description of epidemic dynamics. We also examined the effectiveness of cyclical lockdowns compared to constant-level lockdowns through numerical simulations. Using two different lockdown starting times, $t_{\text{lag}} = 259$ and $t_{\text{lag}} = 289$, we found that cyclical lockdowns with up to five "working days" can suppress the number of active cases. For $t_{\text{lag}} = 259$, constant-level lockdowns consistently achieved lower total incidences than cyclical lockdowns, while for $t_{\text{lag}} = 289$, only the policy of $W6L1$ that outperformed its constant-level counterpart. Additional simulations on subperiod A (low-to-high transmission rates) and subperiod B (high-to-low transmission rates) further revealed that the performance of cyclical versus constant-level lockdowns depends strongly on timing. In subperiod A, cyclical lockdowns ($W6L1$, $W5L2$, $W4L3$, $W3L4$) yielded lower incidences because they avoided over-allocating resources to periods of low transmission. Conversely, in subperiod B, constant-level lockdowns were more effective because they concentrated restrictions during periods of high transmission. These results underscore the importance of lockdown timing.

While prolonged constant-level lockdowns can be epidemiologically effective, they impose heavy social and economic burdens. Furthermore, although we have shown that constant-level lockdown consistently outperformed cyclical lockdown when it is concentrated over period with high transmission rates, it is not simplistic to accurately predict when the transmission rates will be higher than usual. Our simulations show that cyclical lockdowns with three or four lockdown days per week can nearly replicate the effectiveness of continuous lockdowns in terms of both epidemic curves and total incidences. Thus, cyclical lockdowns offer a promising alternative, balancing epidemiological effectiveness with reduced socio-economic costs. We are also aware that cyclical lockdowns may have a logistical cost. Our numerical simulations are intended to explore the efficacy of cyclical lockdown interventions, while real-world practice would require careful consideration of logistical factors.

For further research, the numerical simulation can be done using more intricate and realistic epidemiological models with daily-varying rates and with a different lockdown cycle (i.e. the cycle is every ten days, or two weeks, etc.). Furthermore, instead of applying cyclical lockdowns continuously throughout the entire period, they could be implemented only when necessary. This study does not involve predictive modeling or forecasting; however, future work could explore predictive approaches to estimate when the number of active cases is likely to rise above critical thresholds, triggering the use of cyclical lockdowns. Accurate forecasting would enable more efficient and targeted implementation of short-term cyclical or periodical lockdowns. Future research could also benefit from integrating data-driven forecasting methods with compartmental models. While models like A-SIR provide interpretability and policy simulation capabilities, combining them with modern predictive approaches could support more adaptive and responsive lockdown strategies. Another limitation of the current model is that it does not account for vaccination, since vaccinated individuals are not moved from the susceptible to the recovered compartment. Extending the model to include vaccination would allow for a more accurate representation of real-world conditions. In particular, future research could incorporate vaccination with waning immunity [40], [41] or the emergence of new variants and their effects on immunity. These are critical real-world factors that can shape long-term epidemic outcomes. Nevertheless, the modeling framework remains adaptable. With future updated epidemiological data, the A-SIR model can be recalibrated to better support policy planning for future epidemic waves.

Data and Code Availability

The dataset for cumulative total number of cases and daily active cases were extracted from [30]. The data is then processed using Python software [42]. We use Octave software to run the MVI-estimation algorithm and to do the numerical simulations. Both softwares can be downloaded for free from their official websites. The codes for data processing, MVI estimation, and numerical simulation are publicly available here: https://github.com/anbarief/ICCMM-25-Cyclical-Lockdown/tree/main.

Acknowledgements

The authors would like to acknowledge the anonymous editor and reviewers. This research was supported by Parahyangan Catholic University with the Publikasi Internasional Bereputasi research grant scheme 2025 (Number: III/LPPM/2025-02/22-P).

References

[1] Murphy, C., Lim, W.W., Mills, C., Wong, J.Y., Chen, D., Xie, Y., Li, M., Gould, S., Xin, H., Cheung, J.K., Bhatt, S., Cowling, B.J., and Donnelly, C.A., Effectiveness of social distancing measures and lockdowns for reducing transmission of COVID-19 in non-healthcare, community-based settings, Philosophical Transactions of the Royal Society A: Mathematical, Physical and Engineering Sciences, 381(2257), pp. 1–29, 2023.

[2] Gopinath, G., The great lockdown: worst economic downturn since the great depression, 2020. https://blogs.imf.org/2020/04/14/the-great-lockdown-worst-economic-downturn-since-the-great-depression/, Accessed on February 10, 2025.

[3] Mofijur, M., Fattah, I.R., Alam, M.A., Islam, A.S., Ong, H.C., Rahman, S.A., Najafi, G., Ahmed, S.F., Uddin, M.A. and Mahlia, T.M.I., Impact of COVID-19 on the social, economic, environmental and energy domains: Lessons learnt from a global pandemic, Sustainable Production and Consumption, 26, pp. 343–359, 2021.

[4] Bragazzi, N.L., Han, Q., Iyaniwura, S.A., Omame, A., Shausan, A., Wang, X., Woldegerima, W.A., Wu, J. and Kong, J.D., Adaptive changes in sexual behavior in the high-risk population in response to human monkeypox transmission in Canada can help control the outbreak: Insights from a two-group, two-route epidemic model, Journal of Medical Virology, 95(4), p. e28575, 2023.

[5] Khan, M.A., Dengue infection modeling and its optimal control analysis in East Java, Indonesia, Heliyon, 7(1), 2021.

[6] Kuddus, M.A., Rahman, A., Alam, F. and Mohiuddin, M., Analysis of the different interventions scenario for programmatic measles control in Bangladesh: A modelling study, PLoS One, 18(6), p. e0283082, 2023.

[7] Feng, Y., Iyer, G. and Li, L., Scheduling fixed-length quarantines to minimize the total number of fatalities during an epidemic, Journal of Mathematical Biology, 82(7), p. 69, 2021.

[8] Britton, T. and Leskelä, L., Optimal intervention strategies for minimizing total incidence during an epidemic, SIAM Journal on Applied Mathematics, 83(2), pp. 354–373, 2023.

[9] Flaxman, S., Mishra, S., Gandy, A., Unwin, H.J.T., Mellan, T.A., Coupland, H., Whittaker, C., Zhu, H., Berah, T., Eaton, J.W. and Monod, M., Estimating the effects of non-pharmaceutical interventions on COVID-19 in Europe, Nature, 584(7820), pp. 257–261, 2020.

[10] Bisiacco, M. and Pillonetto, G., COVID-19 epidemic control using short-term lockdowns for collective gain, Annual Reviews in Control, 52, pp. 573-586, 2021.

[11] Bin, M., Cheung, P.Y., Crisostomi, E., Ferraro, P., Lhachemi, H., Murray-Smith, R., Myant, C., Parisini, T., Shorten, R., Stein, S. and Stone, L., Post-lockdown abatement of COVID-19 by fast periodic switching, PLoS Computational Biology, 17(1), p. e1008604, 2021.

[12] Yong, B., Hoseana, J. and Owen, L., 2022. From pandemic to a new normal: Strategies to optimise governmental interventions in Indonesia based on an SVEIQHR-type mathematical model, Infectious Disease Modelling, 7(3), pp. 346–363, 2022.

[13] Saha, S., Samanta, G. and Nieto, J.J., Impact of optimal vaccination and social distancing on COVID-19 pandemic, Mathematics and Computers in Simulation, 200, pp. 285–314, 2022.

[14] Dutta, R., Gomes, S.N., Kalise, D. and Pacchiardi, L., Using mobility data in the design of optimal lockdown strategies for the COVID-19 pandemic, PLoS Computational Biology, 17(8), p. e1009236, 2021.

[15] Hritonenko, N. and Yatsenko, Y., Analysis of optimal lockdown in integral economic–epidemic model. Economic Theory, 77(1), pp. 235–259, 2024.

[16] Fu, Y., Xiang, H., Jin, H. and Wang, N., Mathematical modelling of lockdown policy for Covid-19, Procedia Computer Science, 187, pp. 447–457, 2021.

[17] Acemoglu, D., Chernozhukov, V., Werning, I. and Whinston, M.D., Optimal targeted lockdowns in a multigroup SIR model, American Economic Review: Insights, 3(4), pp. 487–502, 2021.

[18] Vassallo, L., Perez, I.A., Alvarez-Zuzek, L.G., Amaya, J., Torres, M.F., Valdez, L.D., La Rocca, C.E. and Braunstein, L.A., An epidemic model for COVID-19 transmission in Argentina: Exploration of the alternating quarantine and massive testing strategies, Mathematical Biosciences, 346, p. 108664, 2022.

[19] Marinov, T.T. and Marinova, R.S., Adaptive SIR model with vaccination: Simultaneous identification of rates and functions illustrated with COVID-19, Scientific Reports, 12(1), p. 15688, 2022.

[20] Marinov, T.T. and Marinova, R.S., Dynamics of COVID-19 using inverse problem for coefficient identification in SIR epidemic models, Chaos, Solitons & Fractals: X, 5, p. 100041, 2020.

[21] Marinov, T.T., Marinova, R.S., Omojola, J. and Jackson, M., Inverse problem for coefficient identification in SIR epidemic models, Computers & Mathematics with Applications, 67(12), pp. 2218–2227, 2014.

[22] Marinov, T.T. and Marinova, R.S., Coefficient identification in Euler–Bernoulli equation from over-posed data, Journal of Computational and Applied Mathematics, 235(2), pp. 450-459, 2010.

[23] Nadia, A.Z., Rizqina, S., Sukandar, K.K., Fakhruddin, M., Tay, C.J. and Nuraini, N., Data-Driven Generating Operator in SEIRV Model for COVID-19 Transmission, Communications in Biomathematical Sciences, 6(1), pp. 74-89, 2023.

[24] Cheng, C., Aruchunan, E. and Noor Aziz, M.H., Leveraging dynamics informed neural networks for predictive modeling of COVID-19 spread: a hybrid SEIRV-DNNs approach, Scientific Reports, 15(1), p. 2043, 2025.

[25] Ning, X., Jia, L., Wei, Y., Li, X.A. and Chen, F., Epi-DNNs: Epidemiological priors informed deep neural networks for modeling COVID-19 dynamics, Computers in Biology and Medicine, 158, p. 106693, 2023.

[26] Jing, M., Ng, K.Y., Mac Namee, B., Biglarbeigi, P., Brisk, R., Bond, R., Finlay, D. and McLaughlin, J., COVID-19 modelling by time-varying transmission rate associated with mobility trend of driving via Apple Maps, Journal of Biomedical Informatics, 122, p. 103905, 2021.

[27] Girardi, P. and Gaetan, C., An Seir model with time-varying coefficients for analyzing the sars-cov-2 epidemic, Risk Analysis, 43(1), pp. 144–155, 2023.

[28] Kermack, W.O. and McKendrick, A.G., A contribution to the mathematical theory of epidemics, *Proceedings of The Royal Society of London, Series A,* 115(772), pp. 700–721, 1927.

[29] United Nations Department of Economic and Social Affairs, World population prospects 2024: Downloads, 2024. https://population.un.org/wpp/downloads/, Accessed on February 10, 2025.

[30] Worldometer, Worldometer: Real time world statistics, 2025. https://www.worldometers.info/, Accessed on February 10, 2025.

[31] Weisstein, E. W., Delta Function, MathWorld–A Wolfram web resource, n.d. https://mathworld.wolfram.com/DeltaFunction.html, Accessed on February 10, 2025.

[32] Burden, R.L. and Faires, J.D., *Numerical Analysis*, 9th ed., Boston: Cengage Learning, 2010.

[33] Our World in Data, COVID-19 variants data explorer, 2025. https://ourworldindata.org/grapher/covid-variants-area?country=~USA, Accessed on February 10, 2025.

[34] U.S. Department of State, Update on change to U.S. travel policy requiring COVID-19 vaccination for non-immigrant travel, 2023. https://travel.state.gov/content/travel/en/News/visas-news/update-on-change-to-us-travel-policy-requiring-covid-19-vaccination-for-nonimmigrant-travel.html, Accessed on February 10, 2025.

[35] Earnest, R., Uddin, R., Matluk, N., Renzette, N., Turbett, S.E., Siddle, K.J., Loreth, C., Adams, G., Tomkins-Tinch, C.H., Petrone, M.E. and Rothman, J.E., Comparative transmissibility of SARS-CoV-2 variants delta and alpha in New England, USA, Cell Reports Medicine, 3(4), 2022.

[36] Ito, K., Piantham, C. and Nishiura, H., Estimating relative generation times and relative reproduction numbers of Omicron BA. 1 and BA. 2 with respect to Delta in Denmark, Mathematical Biosciences and Engineering, 19, 2022.

[37] Chen, J., Wang, R., Gilby, N.B. and Wei, G.W., Omicron variant (B. 1.1. 529): infectivity, vaccine breakthrough, and antibody resistance, Journal of chemical information and modeling, 62(2), pp. 412–422, 2022.

[38] Tan, M.W., Anelone, A.J., Tay, A.T., Tan, R.Y., Zeng, K., Tan, K.B. and Clapham, H.E., Differences in virus and immune dynamics for SARS-CoV-2 Delta and Omicron infections by age and vaccination histories, BMC Infectious Diseases, 24(1), p. 654, 2024.

[39] Centers for Disease Control and Prevention (CDC), CDC museum COVID-19 timeline, 2025. https://www.cdc.gov/museum/timeline/covid19.html, Accessed on February 10, 2025.

[40] El Khalifi, M. and Britton, T., SIRS epidemics with individual heterogeneity of immunity waning, Journal of Theoretical Biology, 587, p. 111815, 2024.

[41] Khan, M.M.U.R. and Tanimoto, J., Influence of waning immunity on vaccination decision-making: A multi-strain epidemic model with an evolutionary approach analyzing cost and efficacy, Infectious Disease Modelling, 9(3), pp. 657–672, 2024.

[42] Python Software Foundation, Python programming language – official website, 2025. https://www.python.org/, Accessed on February 10, 2025.

[43] GNU Octave Project, GNU Octave – High-level language for numerical computations, 2025. https://www.octave.org/, Accessed on February 10, 2025.